

# Hollow Spherical Hierarchical MoO<sub>3</sub>/SiO<sub>2</sub>-TiO<sub>2</sub> Structures for Photocatalytic Decomposition of Organic Pollutant in Water

**Svetlana A. Kuznetsova**

National Research Tomsk State University

**Olga S. Khalipova**

National Research Tomsk State University

**Konstantin V. Lisitsa**

National Research Tomsk State University

**Liliya A. Selunina**

National Research Tomsk State University

**Victor V. Khasanov**

National Research Tomsk State University

**Alexandra G. Malchik**

National Research Tomsk Polytechnic University

**Yu-Wen Chen** (✉ [ywchen@cc.ncu.edu.tw](mailto:ywchen@cc.ncu.edu.tw))

National Central University

---

## Research Article

**Keywords:** Molybdenum trioxide, Titanium dioxide, Photocatalysis, Methylene blue destruction

**Posted Date:** June 17th, 2022

**DOI:** <https://doi.org/10.21203/rs.3.rs-1737689/v1>

**License:**   This work is licensed under a Creative Commons Attribution 4.0 International License.

[Read Full License](#)

---

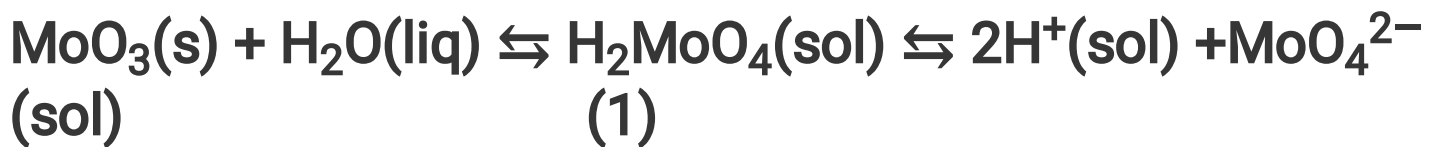
# Abstract

MoO<sub>3</sub>/TiO<sub>2</sub>-SiO<sub>2</sub> layered spherical composites with hierarchical structures have been synthesized via a template and sol-gel methods in which TOKEM-320Y anion exchanger was used as template. The properties of MoO<sub>3</sub>/TiO<sub>2</sub>-SiO<sub>2</sub> spherical composites were characterized by X-ray diffraction, Scanning electron microscopy, Energy-dispersive X-ray spectroscopy, 3D X-ray microtomography, N<sub>2</sub> sorption, Infrared and Raman spectroscopies and ultraviolet spectrophotometry. The photocatalytic activity of MoO<sub>3</sub>/TiO<sub>2</sub>-SiO<sub>2</sub> composites was evaluated by photocatalytic degradation of methylene blue (MB) aqueous solution under irradiated with an I<sub>2</sub> excilamp ( $\lambda_{\text{max}} = 312 \text{ nm}$ ) and its photoabsorption energy properties are related to the interaction between TiO<sub>2</sub>-SiO<sub>2</sub> and MoO<sub>3</sub> which occurs through oxygen in Ti-O-Mo and Si-O-Mo. The layered hierarchical structure results in lower oxygen vacancy concentrations in composites (0.0425) and a reduced bandgap width (2.58 eV in compare to 3.18 eV for MoO<sub>3</sub> spheres), which increases the composite's absorption of light in the visible light regime ( $\lambda$  absorption edge is 480.5 nm). Photocatalytic degradation of the MB dye followed the pseudo-first-order-kinetics. Degradation product analysis was done using the HPLC-MS technique. The dye degradation is initiated by demethylation of the molecule and lead to formation of azure A, B and C and thionin. The results showed that MoO<sub>3</sub>/TiO<sub>2</sub>-SiO<sub>2</sub> composites exhibited a much higher photocatalytic activity (rate constant is 0.0645 min<sup>-1</sup>) than that of MoO<sub>3</sub> spheres and other MoO<sub>3</sub> samples in the literature. This investigation demonstrates that MoO<sub>3</sub>/TiO<sub>2</sub>-SiO<sub>2</sub> layered spherical composites is a promising candidate material for photocatalytic decomposition of organic dyes in textile waste water which are considered as one of the greatest threats to the environment.

## 1. Introduction

The waste water from textile industry is considered as one of the greatest threats to the environment. Disposing of such wastewater without proper treatment creates environmental problems [1, 2]. It has been proposed to solve this problem by photocatalytic decomposition of organic dyes in textile waste water [3]. This method has attracted the attention of scientists due to its simplicity and low cost. Porous semiconductor oxide materials are used as photocatalysts, which show good adsorption properties to organic dyes, photochemical stability and nontoxicity. So far, most researchers have focused on titanium dioxide [4–6]. However, TiO<sub>2</sub> shows photocatalytic properties only under the electromagnetic radiation of the ultraviolet range which accounts for only 5% of the solar spectrum [7], that deal with its large band gap energy (e.g., 3.2 eV for anatase and brookite structures, 3.0 eV for rutile). Titanium dioxide also shows an insufficiently high rate of decomposition of organic dyes [8]. Various methods of increasing the photocatalytic activity of TiO<sub>2</sub> have been reported. These are alloying oxide by other elements to form the solid solutions [9, 10], as well as obtaining multicomponent oxide composites with a hierarchical structure [11, 12], which allows not only to shift the absorption edge into the visible light region of the spectrum, but also to increase the rate of pollutants decomposition. Another semiconductor oxide that has been extensively studied over the last 25 years for photocatalyst

applications was MoO<sub>3</sub> [13, 14]. MoO<sub>3</sub> is one of the most important photocatalysts because of its interesting semiconducting, rich chemistry associated with multiple valence states and high thermal and chemical stability. MoO<sub>3</sub> crystallizes in several modifications: the orthorhombic phase (a-MoO<sub>3</sub>), the metastable monoclinic phase (b-MoO<sub>3</sub>), the hexagonal phase (h-MoO<sub>3</sub>) and the high-pressure monoclinic phase (MoO<sub>3</sub>-II). a-MoO<sub>3</sub> exhibits high photocatalytic activity in the decomposition reactions of organic pollutants [15]. a-MoO<sub>3</sub> has a layered hierarchical structure with an adjustable band gap width. The catalytic properties are explained by the high oxygen activity of the a-MoO<sub>3</sub> crystal lattice and the relatively high specific surface area (from 30 to 60 m<sup>2</sup>/g). a-MoO<sub>3</sub> is an n-type indirect-gap semiconductor [16] with band gap from 2.9 to 3.15 eV in single crystal [17, 18]. Studies indicated that the photocatalytic activity of molybdenum trioxide depends not only on the type of crystal structure, but also on the shape and size of the agglomerate, which consists of nanoparticles of hierarchical structure. The main focus is on hollow spheres consisting of flower-shaped a-MoO<sub>3</sub> nanoparticles constructed from low-dimensional nanoribbons, nanofibers, and nanosheets [19–23]. It has been reported [24, 25] that the addition of titanium dioxide to molybdenum trioxide enhanced the catalytic and photocatalytic activity of the material. The joint action of TiO<sub>2</sub> and MoO<sub>3</sub> catalyst in the oxidation of organic acid consists in the adsorption of acid on the main active center of titanium dioxide (Ti–OH), after which this acid is destroyed on the oxygen of the active center of molybdenum trioxide (Mo–O). In addition, the application of catalyst based on molybdenum(VI) and titanium(IV) oxides gave high yield of the target product (from 70% to 85 % of selectivity) [25]. The catalytic properties of the MoO<sub>3</sub>–TiO<sub>2</sub>–SiO<sub>2</sub> system were reported in the literature [26]. It shows that MoO<sub>3</sub>–TiO<sub>2</sub>–SiO<sub>2</sub> is more active and selective than MoO<sub>3</sub>–SiO<sub>2</sub>, since TiO<sub>2</sub> not only increases the interaction between MoO<sub>3</sub> and SiO<sub>2</sub>, but also increases the dispersion of MoO<sub>3</sub>, which directly enhances the catalytic activity of composite. Despite the fact that these molybdenum oxide structures exhibit photocatalytic activity, they have a significant drawback, i.e., they are soluble in aqueous solutions of organic dyes (1.3 grams per liter at 25 °C):



This leads to the consumption of the photocatalyst and difficulties in assessing its photocatalytic activity, since the change in the dye absorption spectrum in the study of its photocatalytic decomposition in the presence of molybdenum trioxide is also associated with a change in the acidity of the solution.

In the above-mentioned works, it has been shown that there is no leaching of molybdenum during the reaction of catalysis with MoO<sub>3</sub>–SiO<sub>2</sub> nanospheres, leading to a gradual degradation of the catalyst. This fact is confirmed by the absence of colour change in the solution during the reaction, which is observed

during the catalysis with  $\text{MoO}_3\text{-SiO}_2$  dispersed composite when the color of the reaction solution changes to yellow-green due to the dissolving of  $\text{MoO}_3$ . Hence, it is necessary to form a layered hierarchical structure of the composite, in which bonds  $\text{Mo-O-E}$  (E: titanium or silicon) will be present that can lead to reduce the solubility of molybdenum trioxide in aqueous solutions and to preserve of sorption centers of organic pollutants. In addition, the transition of photoelectrons from the energy conduction band of one oxide to the conduction band of another makes it possible to enhance charge separation and increase photocatalytic activity, due to the absorption of solar radiation.

Previously, we have shown the method to obtain nanostructured  $\text{MoO}_3/\text{TiO}_2\text{-SiO}_2$  composites of a hollow spherical shape of the core-shell type by thermal decomposition of anion exchangers saturated with  $\text{Mo}_7\text{O}_{24}^{6-}$  ions and treated with tetrabutoxytitanium (TBT) sol with tetraethoxysilane (TEOS) [27, 28]. These composites are insoluble in water. The hierarchical core-shell structure of spherical composites provides not only high porosity, but also a high concentration of active centers on the surface, that can be dealt with formation of interfacial boundaries of layers in materials. In this study, we investigated the structural features, textural properties and photocatalytic activity of hollow layered spherical  $\text{MoO}_3/\text{TiO}_2\text{-SiO}_2$  composites with hierarchical structure and the spherical  $\text{MoO}_3$  composites in the photodegradation of methylene blue. The influence of the  $\text{MoO}_3/\text{TiO}_2\text{-SiO}_2$  layered structure on the photocatalytic activity of composite was investigated.

## 2. Experimental

### 2.1 Preparation of composites

Hollow spherical  $\text{MoO}_3/\text{TiO}_2\text{-SiO}_2$  composites were obtained by the template and sol-gel methods. The procedure of preparation of  $\text{MoO}_3/\text{TiO}_2\text{-SiO}_2$  composites with spherical shape was proposed by the authors and presented in detail in the previous work [27]. The TOKEM-320Y anion exchanger (Tokem, Russia) in the hydroxyl form was used as a template. The anion exchange resin was loaded into a saturated solution of ammonium pramo-molybdate (Yugraktiv, Russia) for ion exchange of  $\text{OH}^-$  groups with  $\text{Mo}_7\text{O}_{24}^{6-}$ . Then it was dried at  $60\text{ }^\circ\text{C}$  and immersed into the sol of tetrabutoxytitanium (TBT, Acros, USA) with tetraethoxysilane (TEOS, Ecos-1, Russia). At the last stage, the dried samples were annealed at  $350\text{ }^\circ\text{C}$  for 6 h and at  $500\text{ }^\circ\text{C}$  for 5 h. The heating rate of muffle furnace was  $14\text{ deg min}^{-1}$ . For comparison, the  $\text{MoO}_3$  spheres were obtained according to the proposed technique but without the stage of immersing the anion exchanger saturated  $\text{Mo}_7\text{O}_{24}^{6-}$  into the sol. In addition, the  $\text{TiO}_2\text{-SiO}_2$  samples were prepared by only coating the cations with sol TBT-TEOS. The annealing temperatures and the preparation method of all samples were the same.

### 2.2 Characterization

The phase composition and structure of the prepared samples were studied by X-ray diffraction (XRD) using a Rigaku Miniflex 600 (Japan) with a  $\text{CuK}_\alpha$  source ( $\lambda = 1.5418\text{ \AA}$ ) and monochromator. The

diffraction pattern was scanned by steps of  $0.02^\circ$ , recording rate of  $2 \text{ deg min}^{-1}$  in the  $2\theta$  range from  $10^\circ$  to  $90^\circ$ . The qualitative phase composition was determined using the PCPDFWIN database and the full-profile analysis program POWDER CELL 2.4. The crystallite size was calculated using the POWDER CELL 2.4 program and the Scherrer's equation:

$$D_{\text{XRD}} = K\lambda/\beta\cos\theta \quad (2)$$

where  $D_{\text{XRD}}$  is the crystallite size;  $K$  is a dimensionless shape factor with a value close to unity;  $\lambda$  is the X-ray wavelength;  $\beta$  is line broadening at half maximum intensity.

The surface morphology of samples was studied by scanning electron microscopy (SEM). The distribution of elements on the surface was determined by energy dispersive X-ray spectroscopic (EDS) analysis. These analyses were performed on a Hitachi TM-3000 scanning electron microscope with attachment quantax 70 for X-ray microanalysis (Hitachi High-Technologies Corporation, Japan).

The spatial structure of  $\text{MoO}_3/\text{TiO}_2\text{-SiO}_2$  composites with spherical form was investigated by 3D microtomography using a digital 3D X-ray microtomograph developed at Tomsk State University. Samples were placed on a stage located between the detector and the X-ray tube. X-ray power was 80 kV at an emission current of  $50 \mu\text{A}$ . Scanning of the sample resulted in 10,000 shadow projections, which corresponds to a  $180^\circ$  rotation of the sample. Computer 3D reconstruction of the object with obtaining a 3D model and a set of sections was performed using the software developed at the Tomsk State University.

The specific surface, porosity and other textural characteristics of the samples were studied by low-temperature adsorption-desorption  $\text{N}_2$  on a TriStar II Micromeritics device. The specific surface area was determined using the Brunauer-Emmett-Teller (BET) multipoint method in the range of  $P/P_0$  from 0.05 to 0.30. Pore size distribution plots were plotted using the Barrett-Joyner-Haland (BJH) method with adsorption branch isotherm analysis. Before measurements, samples (200 mg) were degassed in vacuum at  $200^\circ\text{C}$  for 2 h.

The IR and Raman spectra of the samples were carried out on a Nicolet 6700 spectrophotometer (USA) in the frequency range from  $400$  to  $4000 \text{ cm}^{-1}$  and Nicolet NXR 9650 spectrophotometer (USA) in the frequency range from  $100$  to  $1300 \text{ cm}^{-1}$ , respectively, to study the formation of the bonds in the composites. The absorptions of aqueous suspensions of  $\text{MoO}_3$  and  $\text{MoO}_3/\text{TiO}_2\text{-SiO}_2$  composites were measured by ultraviolet spectrophotometer PE-5400 UV (Russia) within the wave range of  $220\text{--}1000 \text{ nm}$ . The width of the energy gap in the samples was determined by the edge of the resonance-absorption band in the ultraviolet spectrum. The final absorption spectra were presented in the coordinates of  $\text{Öa} = f(h \times n)$ .

The study of the photocatalytic activity of the samples was carried out on a model reaction of photodegradation of the dye methylene blue (MB) according to the method [29]. The sample of the

catalyst (0.12 g) was placed into quartz flask with 42 ml of MB aqueous solution with concentration of 5 mg/L. The flask was left in the dark for 1 h to reach adsorption equilibrium. After the adsorption-desorption equilibrium was established, the mixture of the organic dye with the sample was irradiated with an I<sub>2</sub> excilamp ( $\lambda_{\text{max}} = 312 \text{ nm}$ ) (model I<sub>2</sub>-BD\_P, Russia). After irradiation every 10 min for 1 h, the aliquots of reaction solution were taken and filtrated and the concentration of MB was determined by an UV-vis spectrophotometer (PE-5400 UV spectrophotometer) in the wavelength range 500–800 nm by the intensity of the absorption maximum at  $\lambda = 664 \text{ nm}$ . To confirm that photolysis and decolorization of the dye did not occur in the MB solution without MoO<sub>3</sub> and MoO<sub>3</sub>/TiO<sub>2</sub>-SiO<sub>2</sub> samples, a blank test was performed, in which the MB solution was kept under the same conditions without catalyst.

The analysis of the products of MB decomposition were carried out using an HPLC-MS system consisting of a Surveyor HPLC system with a PDA Plus diode array detector and an LCQ Advantage MAX mass spectral detector (Thermo, USA). The system was controlled by XCalibur software. The dye degradation products were separated by using Hypersil Gold C18 column 150 mm x 4 mm packed with 5  $\mu\text{m}$  particle size. The mobile phase consisted of two solutions. Solution A was 0.4% HCOOH in water, whereas solution B was acetonitrile. The gradient elution was from 10% to 90% acetonitrile in 10 min, the flow rate was 0.5 mL/min and the injection volume was 10  $\mu\text{l}$ . The temperature of the column thermostat was 22 °C. The conditions of analysis were as follows: UV scanning was from 200 to 400 nm, mass spectrometer was equipped with cationic electrospray (ESI +), capillary voltage was 3.5 kV, mass range was from 50 to 700 m/z, the drying temperature was 250 °C. Nitrogen gas was used as a collision gas (3 and 15 units).

## 3. Results And Discussion

### 3.1 Composition and textural characteristics of MoO<sub>3</sub> and MoO<sub>3</sub>/TiO<sub>2</sub>-SiO<sub>2</sub> samples

The XRD patterns of all three samples are shown in Fig. 1. According to the XRD results, samples 1 and 2 include  $\alpha$ -MoO<sub>3</sub> of orthorhombic modification. The orthorhombic phase  $\alpha$ -MoO<sub>3</sub> has a layered structure consisting of double layers of MoO<sub>6</sub> octahedra with covalent bonds in planes (100) and (001), and van der Waals forces between layers in direction (010). In the double-layer structure, oxygen is bound to a single molybdenum sticking out from both sides of the double layer [30]. The interaction between the layers is much weaker than the interaction between the molybdenum and oxygen inside the layer. The unit cell parameters of  $\alpha$ -MoO<sub>3</sub> are  $a = 3.964 \text{ \AA}$ ,  $b = 13.863 \text{ \AA}$  and  $c = 3.696 \text{ \AA}$  for sample 1 (MoO<sub>3</sub>/TiO<sub>2</sub>-SiO<sub>2</sub> composites) and  $a = 3.961 \text{ \AA}$ ,  $b = 13.869 \text{ \AA}$ ,  $c = 3.699 \text{ \AA}$  for sample 2 (MoO<sub>3</sub> sphere). The average crystallite size of samples 1 and 2 are 256  $\text{\AA}$  and 384  $\text{\AA}$ , respectively. The lack of possibility to detect diffraction maxima belonging to titanium dioxide of anatase structure on the diffractogram of MoO<sub>3</sub>/TiO<sub>2</sub>-SiO<sub>2</sub> sample (Fig. 1, sample 1) may be due to both the small amount of this oxide and the fact that its most intense peak appears at the same angles as those of molybdenum trioxide. The

presence of silicon oxide in the  $\text{MoO}_3/\text{TiO}_2\text{-SiO}_2$  composites does not confirm by XRD, that can be due to the small amount of  $\text{SiO}_2$ .

The  $\text{TiO}_2\text{-SiO}_2$  sample is  $\text{TiO}_2$  of anatase structure (Fig. 1, sample 3) with the parameters:  $a = b = 3.776 \text{ \AA}$ ,  $c = 9.418 \text{ \AA}$ . Wide diffraction peaks in the X-ray patterns confirm the low degree of crystallinity of this sample, that probably deals with the presence of X-ray-amorphous silicon dioxide. The presence of  $\text{SiO}_2$  in the sample 3 is proved by the results of EDS analysis. As can be seen from the X-ray emission spectrum of  $\text{TiO}_2\text{-SiO}_2$  sample (Fig. 2, a), silicon is present in addition to Ti and O.

EDS analysis of  $\text{MoO}_3/\text{TiO}_2\text{-SiO}_2$  sample (Fig. 2, b) also indicates the presence of Si and Ti in addition to Mo and O elements, that confirms the presence not only molybdenum oxide, but also titanium oxide and silicon oxide in this sample.

The results of SEM indicate that the samples had a spherical shape with the same size as that of the TOKEM-320 anion exchanger, which was used as the template (Fig. 3).

$\text{MoO}_3$  and  $\text{MoO}_3/\text{TiO}_2\text{-SiO}_2$  spheres consisted of rod-like structure agglomerates with the length from 1 to 7  $\mu\text{m}$ , which indicates the aggregation of crystallites (data from the Scherrer's Eq.  $256 \text{ \AA}$  and  $384 \text{ \AA}$ ). The morphology of the connected microrods indicates that the microcrystals of these samples had a hierarchical structure. However, significant morphological changes between samples depending on their composition were not observed. The results of 3D computer microtomography confirm that the  $\text{MoO}_3/\text{TiO}_2\text{-SiO}_2$  spherical composites are hollow inside. Two structures can be visually distinguished in Fig. 4, the dark color refers to the air-filled cavity of the sphere, and the lighter color refers to the oxide skeleton of spherical composites.

The layering of the hierarchical spherical structure is proved by the results of qualitative X-ray microanalysis of the composite in section (Fig. 5). As can be seen from the distribution of Mo, O and Ti elements, the molybdenum trioxide constitutes the core of the sphere, and  $\text{TiO}_2\text{-SiO}_2$  composite is the shell in the form of a thin layer. The element Si in the distribution profile was not observed due to its low initial amount in the sol.

The  $\text{MoO}_3$  and  $\text{MoO}_3/\text{TiO}_2\text{-SiO}_2$  spheres can be attributed to mesoporous samples. As shown in Fig. 6a, the adsorption/desorption isotherm of the  $\text{MoO}_3$  samples show that they are mesoporous materials. The same pattern was observed for  $\text{MoO}_3/\text{TiO}_2\text{-SiO}_2$  samples. The coating of the spherical  $\text{MoO}_3$  core by the  $\text{TiO}_2\text{-SiO}_2$  layer did not lead to changes in the type of sorption, porosity and specific surface area ( $5.8 \text{ m}^2/\text{g}$ ) of the samples (Fig. 6).

IR spectra of the spherical  $\text{MoO}_3$  and  $\text{MoO}_3/\text{TiO}_2\text{-SiO}_2$  samples are shown in Fig. 7. The absorption bands corresponding to water and oxygen molecules adsorbed from the air on the surface of the samples were not detected in the IR spectra.

The spectrum of  $\text{MoO}_3$  contains two intense and two weak peaks of valence vibrations of molybdenum–oxygen bonds of the oxide crystal structure. Short  $[\text{Mo} = \text{O}]$  double bond appears as a band at  $970 \text{ cm}^{-1}$ . IR absorptions at  $812$  and  $825 \text{ cm}^{-1}$  refer to the valence vibrations of the  $[\text{Mo}–\text{O}–\text{Mo}]$  bridge bonds. The assignment of the bond vibrational bands was performed in accordance with the literature data [31]. In the IR spectrum of the  $\text{MoO}_3/\text{TiO}_2\text{–SiO}_2$  sample (Fig. 7, b) vibrations of bonds belonging to  $[\text{Ti}–\text{O}]$  of the  $\text{TiO}_2$  matrix at  $430$  and  $500 \text{ cm}^{-1}$  are not observed [32]. The absorptions around  $800, 960 \text{ cm}^{-1}$ , which refer to the  $[\text{Si}–\text{O}–\text{Si}]$  bond vibrations and  $[\text{Si}–\text{O}–\text{Ti}]$  heterobonding vibrations [33, 34], respectively, was not detected, since they overlap with the region of molybdenum–oxygen bond vibrations [35, 36]. However, the shift of  $[\text{Mo} = \text{O}]$  vibration at  $978 \text{ cm}^{-1}$  as well as  $[\text{Mo}–\text{O}–\text{Mo}]$  vibrations at  $825$  and  $855 \text{ cm}^{-1}$  to a higher frequency region indirectly indicates the presence of these bonds.

The comparison of the IR spectra of the samples shows that the only one difference among them is the pronounced absorption maximum at  $1099 \text{ cm}^{-1}$  in the spectrum of  $\text{MoO}_3/\text{TiO}_2\text{–SiO}_2$  composites (Fig. 7, b). According to the literature data, these absorption bands can be attributed to the  $[\text{Si}–\text{O}–\text{Mo}]$  bond vibrations.

The Raman spectra of the samples are shown in Fig. 8. The Raman active modes were identified in accordance to the literature data [37] and confirmed the orthorhombic phase of  $\text{MoO}_3$ . The similarity of the Raman spectra of  $\text{MoO}_3$  and  $\text{MoO}_3/\text{TiO}_2\text{–SiO}_2$  samples indicates that the crystal structure of molybdenum trioxide is preserved during the formation of  $\text{TiO}_2\text{–SiO}_2$  layer on it. In the spectrum of  $\text{MoO}_3/\text{TiO}_2\text{–SiO}_2$  composite in addition to the  $\text{MoO}_3$  modes, the most intense Raman peaks of the  $\text{TiO}_2$  structure of anatase at  $114.0, 126.8, \text{ and } 153.9 \text{ cm}^{-1}$  are present. Such a number of modes can be explained by the fact that the  $\text{TiO}_2$  consists of particles of different sizes and the shift of the frequencies of these modes to the long-wavelength region indirectly indicates the formation of a bond  $\text{Mo}–\text{O}–\text{Ti}$ .

Full width change at half maximum (FWHM) of the Raman peak at  $819 \text{ cm}^{-1}$  in the  $\text{MoO}_3/\text{TiO}_2\text{–SiO}_2$  sample compared to the FWHM of the Raman peak at  $819 \text{ cm}^{-1}$  in the  $\text{MoO}_3$  sample (Fig. 8) indicates that the defectiveness of the  $\text{MoO}_3$  structure in these samples is different. As can be seen from Fig. 8, FWHM decreases from  $\text{MoO}_3$  sample to  $\text{MoO}_3/\text{TiO}_2\text{–SiO}_2$  sample. This indicates a greater number of oxygen vacancies in the  $\text{MoO}_3$  than in the  $\text{MoO}_3/\text{TiO}_2\text{–SiO}_2$  sample. The intensity ratio of Raman modes at  $282\text{–}290 \text{ cm}^{-1}$  and the equation ( $x = 0.01296R + 2.93429$ ) obtained from Dieterle's data [38] were used to determine the oxygen stoichiometry in  $\text{MoO}_{3-x}$ . Table 1 shows that the  $\text{MoO}_3$  sample has more vacancies compared to the  $\text{MoO}_3/\text{TiO}_2\text{–SiO}_2$  sample. This result is consistent with the FWHM of the Raman peak at  $819 \text{ cm}^{-1}$ .

Table 1

Values of the ratio of intensity of the Raman peaks at 282–290  $\text{cm}^{-1}$  with their respective oxygen vacancies.

Sample	$R(I_{283}/I_{290})$	$R(I_{282}/I_{289})$	Oxygen index x ( $\text{MoO}_x$ )	Oxygen vacancy
$\text{MoO}_3$	1.6538	-	2.9556	0.0444
$\text{MoO}_3/\text{TiO}_2\text{-SiO}_2$	-	1.4166	2.9525	0.0425

Consequently,  $\text{MoO}_3/\text{TiO}_2\text{-SiO}_2$  sample (sample 1) is a composite of  $\alpha\text{-MoO}_3$ , anatase phase of  $\text{TiO}_2$  and amorphous phase of  $\text{SiO}_2$  and sample 2 is  $\alpha\text{-MoO}_3$ . The formation of hierarchical layered spherical  $\text{MoO}_3/\text{TiO}_2\text{-SiO}_2$  composites of shell/core type by obtained by template and sol-gel methods at 500 °C using TOKEM-320Y occurs through the formation of interphase boundaries between orthorhombic phase of  $\text{MoO}_3$  and  $\text{TiO}_2\text{-SiO}_2$  composite which consists of  $\text{TiO}_2$  of tetragonal structure and amorphous phase of  $\text{SiO}_2$ , and formation of Ti–O–Mo and Si–O–Mo chemical bonds. The use of the sol based on tetrabutoxytitanium with tetraethoxysilane contributes to obtaining the regular (dense)  $\text{TiO}_2\text{-SiO}_2$  coating on the spherical hollow core of  $\text{MoO}_3$ . The  $\text{TiO}_2\text{-SiO}_2$  layer reduces the number of oxygen vacancies in the  $\text{MoO}_3$  structure.

## 3.2 Photocatalytic properties of $\text{MoO}_3$ and $\text{MoO}_3/\text{TiO}_2\text{-SiO}_2$ samples

UV–visible spectroscopy was used to study the light absorption properties of samples (Fig. 9A). The experimental results of absorptions measurements of  $\text{MoO}_3$ ,  $\text{TiO}_2\text{-SiO}_2$  and  $\text{MoO}_3/\text{TiO}_2\text{-SiO}_2$  suspensions were analyzed by the function  $(\alpha \cdot h \cdot \nu)^2 = A^2(h \cdot \nu - \Delta E_g)$  [39]. Experimental results of measurements of the dependence  $\alpha$  from  $h \cdot \nu$  for indirect inter band transitions are represented as plots of  $\sqrt{\alpha}$  versus  $h \cdot \nu$  (Fig. 9B), and a scheme for determining the optical bandgap energy ( $\Delta E_g$ ) of  $\text{MoO}_3$ ,  $\text{TiO}_2\text{-SiO}_2$  and  $\text{MoO}_3/\text{TiO}_2\text{-SiO}_2$  samples was also plotted.

Figure 9 shows that the  $\text{MoO}_3$  sample demonstrates stronger absorption intensity than the  $\text{MoO}_3/\text{TiO}_2\text{-SiO}_2$  sample in the hard ultraviolet region. The absorption of  $\text{MoO}_3$  sample decreases if it is covered by the  $\text{TiO}_2\text{-SiO}_2$  layer, that is probably the result of the fundamental process of the formation of an electron–hole pair upon irradiation [40]. The  $\text{MoO}_3/\text{TiO}_2\text{-SiO}_2$  composite absorbs more light than the  $\text{MoO}_3$  sample in the soft ultraviolet region. The determined  $\Delta E_g$  values are 3.18, 2.33 and 2.58 eV for  $\text{MoO}_3$ ,  $\text{TiO}_2\text{-SiO}_2$  and  $\text{MoO}_3/\text{TiO}_2\text{-SiO}_2$  samples, respectively. These values indicate that the formation of  $\text{TiO}_2\text{-SiO}_2$  layer on  $\text{MoO}_3$  core leads to a decrease in the bandgap energy.

The photocatalytic activity of  $\text{MoO}_3$  and  $\text{MoO}_3/\text{TiO}_2\text{-SiO}_2$  was investigated in the degradation of methylene blue (MB) under light irradiation. The results of photocatalytic measurements are presented in Fig. 10. As can be seen in Fig. 10A, the color and absorption intensity of the pure dye change little with

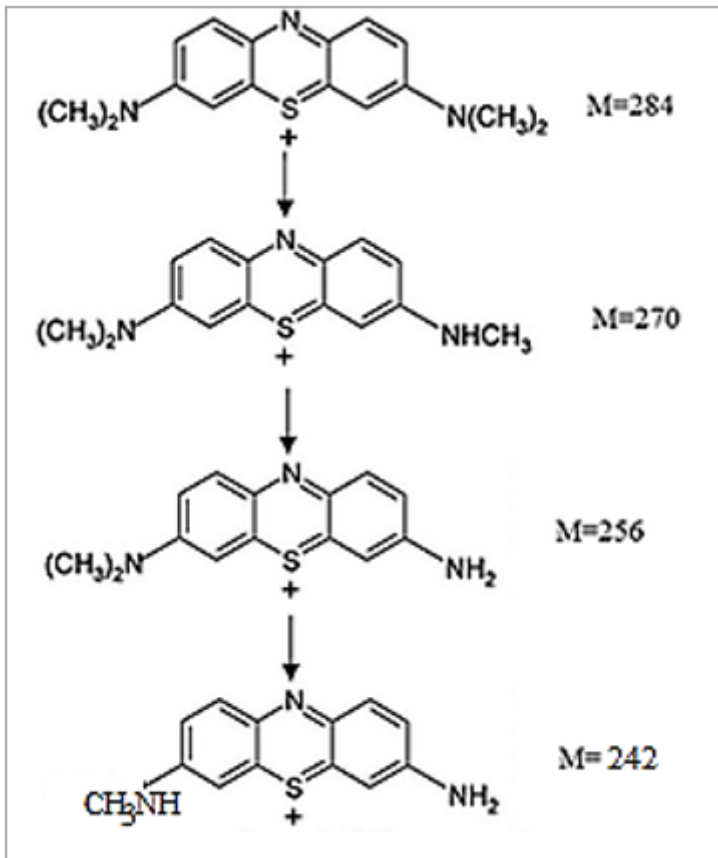
increasing irradiation time. The degree of degradation of pure MB reaches 14 wt. % in 120 min of irradiation with wave length at 312 nm. Keeping the MB with photocatalysts in the dark leads to the sorption of the dye on the surface of samples. The MoO<sub>3</sub> composite adsorbed 76 wt. % of MB during 60 min while the MoO<sub>3</sub>/TiO<sub>2</sub>-SiO<sub>2</sub> composite adsorbed 82 wt.%. It can be explained by the fact that at equal pore diameters the volume of pores in the MoO<sub>3</sub>/TiO<sub>2</sub>-SiO<sub>2</sub> composite is larger than in the MoO<sub>3</sub> sample (Fig. 6). The change in the absorption spectrum of MS solution (Fig. 10B, C) indicates that the dye can undergo degradation in the presence of both samples.

As can be seen in Fig. 11, the photocatalytic decomposition of MB occurred for 40 min in the presence of MoO<sub>3</sub> sample and for 20 min in the presence of MoO<sub>3</sub>/TiO<sub>2</sub>-SiO<sub>2</sub> composite. The linear relationship between  $-\ln(C/C_0)$  and irradiation time can be describe by pseudo-first-order kinetics ( $-\ln(C/C_0) = -kt$ ). The good linearity of the curves confirmed the applicability of this mode with a correlation coefficient value of 0.9621–0.9687 as shown in Fig. 11. Calculated values of the rate constants from the slope of the plot indicate that the rate of decomposition of MB in the presence of MoO<sub>3</sub>/TiO<sub>2</sub>-SiO<sub>2</sub> ( $k = 0.0645 \text{ min}^{-1}$ ) is about 2 times higher than that in the presence of MoO<sub>3</sub> ( $k = 0.0336 \text{ min}^{-1}$ ).

Chromatograms of MB solution after holding it in the dark in the presence of the catalyst (Fig. 12, a) showed no presence of peaks at lower retention times. This result indicates that only sorption of MB on the catalyst surface occurs in the dark. Chromatograms of MB solution in the presence of catalysts after UV light irradiation with wave length at 312 nm indicate that the discoloration of the solution is associated with a change in the structure of the organic dye (Fig. 12, b, c). This is evident by the decrease in the MB peak intensity at retention times of 12.12 min and 17.54 min and the appearance of new peaks detected at lower retention times, which correspond to new photocatalytic products of the dye. The comparison of the chromatographic separation spectra of MB solutions in the presence of different catalysts after irradiation showed (Fig. 12b, c) that MB practically does not remain in present of MoO<sub>3</sub>/TiO<sub>2</sub>-SiO<sub>2</sub> samples. This result confirms the results of study the photocatalytic activity of samples by spectrophotometry.

Further analysis was done by mass spectroscopic (MS) studies of the degradation intermediate products of MB solution after irradiation in present of MoO<sub>3</sub>/TiO<sub>2</sub>-SiO<sub>2</sub> sample and the results are shown in Fig. 13. In mass spectrum of the major detected degradation intermediates eluting at 12.8 min peak with  $m/z = 283.9$  was observed which corresponds to the molar mass of the initial MB. It was not possible to separate the MB degradation intermediates eluting at 2.7 min, because they gather in one peak.

However, by mass spectrometry it was possible to record mass fragments with  $m/z = 270.8, 256.4$  and  $241.5$ , which indicate the presence of intermediate products of MB decomposition:



The formation of azure A, B and C and thionin through the demethylation cleavage during the photocatalytic degradation of MB agree with those reported in the literature [41].

Possible mechanism of photocatalytic actions can be assumed by determining the band structures of the components of the  $\text{MoO}_3/\text{TiO}_2\text{-SiO}_2$  composite. The valance band (VB) and conduction band (CB) potentials of the semiconductor can be calculated using the following empirical equations [42]:

$$E_{VB} = X + 0,5E_g - E_e$$

;

$$E_{CB} = E_{VB} - E_g$$

;

$$X = \left( X(A)^a X(B)^b \right)^{\frac{1}{a+b}}$$

,

where  $E_{VB}$  is the VB edge potential, X is the electronegativity of the semiconductor (a and b are the atomic number of compounds),  $E_e$  is the energy of free electrons vs hydrogen (4.5 eV),  $E_g$  is the band gap energy

of the semiconductor, and  $E_{CB}$  is the CB edge potential.

The results of calculating of the band gap, valence and conductivity band potentials of  $\text{MoO}_3/\text{TiO}_2\text{-SiO}_2$  are presented in Fig. 14.

The CB potential of  $\text{MoO}_3$  is  $-0.89$  eV and more negative than that of  $\text{TiO}_2\text{-SiO}_2$  ( $-0.46$  eV). Hence there is diffusion of electrons from the CB of  $\text{MoO}_3$  to  $\text{TiO}_2\text{-SiO}_2$ . At the same time, there is transfer of holes from the VB of  $\text{TiO}_2\text{-SiO}_2$  ( $2.79$  eV) to  $\text{MoO}_3$  ( $2.29$  eV) because the valence band potential of the former is more positive than that of the latter. Thus the photogenerated electrons and holes are efficiently separated at the heterojunctions. The separated electrons released and the resulting holes are involved in the oxidation process of MB.

## 4. Conclusions

This paper shows the formation of hierarchical structures of layered spherical  $\text{MoO}_3/\text{TiO}_2\text{-SiO}_2$  composites with core/shell type, where the core is an  $\alpha\text{-MoO}_3$  sphere and the shell is  $\text{TiO}_2$  anatase with  $\text{SiO}_2$  amorphous, which are linked through oxygen: Ti-O-Mo and Si-O-Mo. This structure results in lower oxygen vacancy concentrations in  $\text{MoO}_3$  (0.0425) and a reduced bandgap width ( $2.58$  eV), which increases the composite's absorption of light in the visible light regime ( $\lambda$  absorption edge =  $480.5$  nm). The photogenerated electrons and holes are separated at the heterojunctions and are involved in the MB oxidation process and the  $\text{MoO}_3/\text{TiO}_2\text{-SiO}_2$  composites exhibit higher photocatalytic activity as compared to  $\text{MoO}_3$ . A significant improvement of the rate constant ( $k = 0.0645 \text{ min}^{-1}$ ) was achieved, not only compared to the  $\text{MoO}_3$  studied in this study, but also to other  $\text{MoO}_3$  samples in the literature [43, 44]. The higher photodestruction of MB on  $\text{MoO}_3/\text{TiO}_2\text{-SiO}_2$  composite was confirmed by HPLC method. The mechanism of photocatalytic reaction has been proposed. This work shows that the  $\text{MoO}_3/\text{TiO}_2\text{-SiO}_2$  heterostructure allows increasing the photocatalytic performance of the composite, and it is an alternative option for practical applications.

## Declarations

Ethics approval and consent to participate: Authors are required to confirm that the appropriate ethics review and informed consent/animal welfare protocols have been followed.

Consent for publication: All authors have agreed to publish this paper.

Availability of data and materials: Yes. We can provide the original data and materials.

Competing interests: There is not competing interest.

Funding: This research was funded by Ministry of Science and Higher Education of the Russian Federation, project no. FSWM-2020-0037.

## Authors' contributions

Svetlana A. Kuznetsova – Conceptualization, Methodology, Writing - original draft preparation

Olga S. Khalipova – Writing - original draft preparation

Konstantin V. Lisitsa - Formal analysis and investigation

Liliya A. Selunina - Formal analysis and investigation

Victor V. Khasanov – Methodology, Formal analysis and investigation

Alexandra G. Malchik - Formal analysis and investigation

Yu-Wen Chen - Writing - review and editing

## Acknowledgements

This work was performed within the framework of the government assignment of the Ministry of Science and Higher Education of the Russian Federation, project no. FSWM-2020-0037.

## References

1. Madhav, S.; Ahamad, A.; Singh, P.; Mishra, P.K. A review of textile industry: wet processing, envial impacts, and effluent treatment methods. *Environ. Qual. Manag.* **2018**, *27*, 31–41. DOI: 10.1002/tqem.21538.
2. Kamal, A.K.I.; Ahmed, F.; Hassan, M.; Uddin, M.K.; Hossain, S.M. Characterization of Textile Effluents from Dhaka Export Processing Zone (DEPZ) Area in Dhaka, Bangladesh. *Pollution.* **2016**, *2(2)*, 153-161. [https://jpoll.ut.ac.ir/article\\_56944\\_7514.html](https://jpoll.ut.ac.ir/article_56944_7514.html).
3. Frank, S.N.; Bard, A.J.; Frank, S.N.; Bard, A.J. Heterogeneous photocatalytic oxidation of cyanide and sulfite in aqueous solutions at semiconductor. *Powders.* **1977**, *81*, 1484–1488. DOI: 10.1021/j100530a011.
4. Yang, H.; · Li, M.; Li, S.; Tao, A.; Wu, Y. A critical structured TiO<sub>2</sub> with enhanced photocatalytic activity during the formation of yolk-shell structured TiO<sub>2</sub>. *J. Mater. Sci. - Mater. Electron.* **2020**, *31*, 2–9. DOI: 10.1007/s10854-018-9986-z.
5. Chang, Y.; Han, W.; Cui, Sh.; Cai A. Cellulose-inspired synthesis of hierarchically nanostructured TiO<sub>2</sub> with high photocatalytic activity. *Chem. Phys. Lett.* **2020**, *745*, 137249. DOI: 10.1016/j.cplett.2020.137249.
6. Zhang, B.; Cao, Sh.; Du, M.; Ye, X.; Wang Yu.; Ye J. Titanium Dioxide (TiO<sub>2</sub>) Mesocrystals: Synthesis, Growth Mechanisms and Photocatalytic Properties. *Catalysts.* **2019**, *9*, 91. DOI: 10.3390/catal9010091.

7. Pelaez, M.; Nolan, N.T.; Pillai, S.C.; Seery, M.K.; Falaras, P.; Kontos, A.G.; Dunlop, P.S.M.; Hamilton, J.W.J.; Byrne, J.A.; O'Shea, K.; et al. A review on the visible light active titanium dioxide photocatalysts for environmental applications. *Appl. Catal. B Environ* **2012**, 125, 331–349. DOI: 10.1016/j.apcatb.2012.05.036.
8. Gao, M.; Zhu, L.; Song, W.; Wang, J.; Ho, G.W. Structural design of TiO<sub>2</sub>-based photocatalyst for H<sub>2</sub> production and degradation applications. *Catal. Sci. Technol.* **2015**, 5, 4703–4726. DOI: 10.1039/C5CY00879D.
9. Nguyen-Le, M.T.; Lee, B. K. Effective photodegradation of dyes using in-situ N-Ti<sup>3+</sup> co-doped porous titanate-TiO<sub>2</sub> rod-like heterojunctions. *Catal. Today* **2017**, 297, 228–236. DOI: 10.1016/j.cattod.2017.03.036.
10. Wang, Y.; Ma, H.; Guo, J.; Han, Yu; Ding, X.; Zhang, Ya. TiO<sub>2-x</sub> nanoparticles dispersed in center-radial channels of dendritic mesoporous silica nanospheres (DMSNs) as novel structured photocatalysts. *J. Mater Sci.* **2021**, 56, 14659–14671. DOI: 10.1007/s10853-021-06049-z.
11. Yuelin, Wei; Yunfang, Huang; Yu, Fang; Yuezhu, Zhao; Dan, Luo; Qiyao, Guo; Leqing, Fan; Jihuai, Wu Hollow mesoporous TiO<sub>2</sub>/WO<sub>3</sub> sphere heterojunction with high visiblelight-driven photocatalytic activity. *Mater. Res. Bull.* **2019**, 119, 110571. DOI: 10.1016/j.materresbull.2019.110571.
12. Stelzer, J.B.; Caro, J.; Habel, D.; Feike E., Schubert, H.; Fait, M.; Hidde G. Hierarchical nano-structuring of metal oxide catalysts – Part 1: Influence of nano-structuring in the activity of the catalysts. *Chem. Eng. Technol.* **2004**, 27, 8, 839–843. DOI: 10.1002/ceat.200403170.
13. Cheng, L.; Shao, M.; Wang, X.; Hu, H. Single-crystalline molybdenum trioxide nanoribbons: photocatalytic, photoconductive, and electrochemical properties. *Chem. Eur. J.* **2009**, 15, 2310. DOI: 10.1002/chem.200802182.
14. Chernova, N.A.; Roppolo, M.; Dillon, A.C.; Whittingham, M.S. Layered vanadium and molybdenum oxides: batteries and electrochromics. *J. Mater. Chem.* **2009**, 19, 2526. DOI: 10.1039/b819629j.
15. Zhu, Yu.; Yao, Yu.; Luo, Z.; Pan, Ch.; Yang, J.; Fang, Y.; Deng, H.; Liu, Ch.; Tan, Q.; Liu, F.; Guo, Ya. Nanostructured MoO<sub>3</sub> for Efficient Energy and Environmental Catalysis. *Molecules* **2020**, 25, 18. DOI: 10.3390/molecules25010018.
16. Pichat P; Mozzanega, M.N.; Hoang-Van, C. Room Temperature Photoassisted Formation of Hydrogen Molybdenum Bronzes with Alcohol as Hydrogen Source. *Phys. Chem.* **1988**, 92, 464–467. DOI: 10.1021/j100313a044.
17. Erre, R.; Legay, M.H.; Fripiat, J.J. Reaction of Molecular Hydrogen with the 100 Face of MoO II. *Surf. Sci.* **1983**, 127, 69–75. DOI:
18. Deb, S.; Khoc, R. Physical Properties of a Transition Metal Oxide: Optical and Photoelectric Properties of Single Crystal and Thin Film Molybdenum Trioxide. *Proc. R. SOC. Lond. A.* **1968**, 304, 211–231. DOI: 10.1098/rspa.
19. Zhang, J.; Song, P.; Li, J.; Yang, Zh.; Wang, Q. Template-assisted synthesis of hierarchical MoO<sub>3</sub> microboxes and their high gas-sensing performance. *Sens. Actuators B* **2017**, 249, 458–466. DOI:

- 10.1016/j.snb.2017.04.137.
20. Xia, Yu.; Wu, Ch.; Zhao, N.; Zhang, Y. Spongy MoO<sub>3</sub> hierarchical nanostructures for excellent performance ethanol sensor. *Mater. Lett.* **2016**, 171, 117–120. DOI: 10.1016/j.matlet.2015.12.159.
  21. Yan, H.; Song, P.; Zhang, S.; Yang, Zh.; Wang Q. Facile fabrication and enhanced gas sensing properties of hierarchical MoO<sub>3</sub> nanostructures. *RSC Adv.* **2015**, 5(89), 72728–72735. DOI: 10.1039/C5RA13036K.
  22. Wang, Sh.; Zhang, Ya.; Ma, X.; Wang, W.; Li, X.; Zhang, Z.; Qian, Y. Hydrothermal route to single crystalline  $\alpha$ -MoO<sub>3</sub> nanobelts and hierarchical structures. *Solid State Commun.* **2005**, 136(5), 283–287. DOI: 10.1016/j.ssc.2005.08.002.
  23. Yu, X.; Zhang, Gu.; Lu, Zh.; Liu, J.; Lei, X.; Sun, X. Green sacrificial template fabrication of hierarchical MoO<sub>3</sub> nanostructures. *CrystEngComm.* **2014**, 16(19), 3935–3939. DOI: 10.1039/C3CE42251H.
  24. Grabowski, R.; Grzybowska, B.; Samson, K.; Słoczyński, J.; Stoch, J.; Wcisło, K. Effect of Alkaline Promoters on Catalytic Activity of V<sub>2</sub>O<sub>5</sub>–TiO<sub>2</sub> and MoO<sub>3</sub>–TiO<sub>2</sub> Catalysts in Oxidative Dehydrogenation of Propane and in Isopropanol Decomposition. *Appl. Catal., A: General* **1995**, 125(1), 129–144.
  25. Liu, K.; Huang, X.; Pidko, E.A.; Hensen, E.J.M. MoO<sub>3</sub>–TiO<sub>2</sub> synergy in oxidative dehydrogenation of lactic acid to pyruvic acid. *Green Chemistry* **2017**, 19, 3014–3022. DOI: 10.1039/C7GC00807D.
  26. Kuwahara, Ya.; Furuichi, N.; Seki, H.; Yamashita, H. One-pot synthesis of molybdenum oxide nanoparticles encapsulated in hollow silica spheres: an efficient and reusable catalyst for epoxidation of olefins. *J. Mater. Chem. A.* **2017**, 5, 18518–18529. DOI: 10.1039/C7TA06288E.
  27. Kuznetsova, S.A.; Khalipova, O.S.; Lisitsa, K.V.; Chen, Y.-W.; Kozik, V.V.; Ditts, A.A.; Malchik, A.G. Fabrication of MoO<sub>3</sub>/TiO<sub>2</sub>–SiO<sub>2</sub> with hollow spherical shape using resin as the template: effect of decomposition of resins. *J. Appl. Polym. Sci.* **2021**, 50851. DOI: 10.1002/app.50851.
  28. (28) Kuznetsova, S.A.; Khalipova, O.S.; Lisitsa, K.V.; Ditts, A.A.; Malchikm A.G.; Kozik, V.V. Synthesis of nanostructured composite materials of MoO<sub>3</sub>/TiO<sub>2</sub>–SiO<sub>2</sub> with spherical shape prepared with resins. *Nanosystems: Physics, Chemistry, Mathematics* **2021**, 12(2), 232–245. DOI: 10.17586/2220-8054-2021-12-2-232-245.
  29. Kuznetsova, S.A.; Pichugina, A.A.; Kozik, V.V. Microwave-assisted hydrothermal process for the preparation of SnO from an ammoniacal Sn<sub>6</sub>O<sub>4</sub>(OH)<sub>4</sub> suspension. *Inorg. Mater.* 2015, 51, 5, 436–440. DOI: 10.1134/S002016851504007X.
  30. Radha, S.K.; Crowley, K.; Holler, B.A.; Gao, X.P.A.; Lambrecht, W.R.L.; Volkova, H.; Berger, M.-H.; Pentzer, E.; Pachuta, K.G.; Sehirlioglu, A. Ultrathin 2D-oxides: A perspective on fabrication, structure, defect, transport, electron, and phonon properties. *J. Appl. Phys.* **2021**, 129, 220903-1-220903-28. DOI: doi.org/10.1063/5.0051093.
  31. Singh, A.; Kumar, S.; Ahmed, B.; Singh, R.K.; Ojha, A.K. Temperature induced modifications in shapes and crystal phases of MoO<sub>3</sub> for enhanced photocatalytic degradation of dye waste water pollutants under UV irradiation. *J. Alloys Compd.* **2019**, 806, 1368-1376. DOI: 10.1016/j.jallcom.2019.07.272.

32. Krivtsov, I. A.; Ilkaeva, M.; Avdin, V.; Khainakov, S.; Garcia, J.R.; Ordóñez, S.; Díaz, E.; Faba, L. Hydrothermal Peroxo Method for Preparation of Highly Crystalline Silica-Titania Photocatalysts. *J. Colloid Interface Sci.* **2015**, 444, 87–96. DOI: 10.1016/j.jcis.2014.12.044.
33. Davis, R.J.; Liu, Z. Titania–silica: a model binary oxide catalyst system. *Chem. Mater.* **1997**, 9, 2311–2324. DOI: 10.1021/cm970314u.
34. Innocenzi, P. Infrared spectroscopy of sol–gel derived silica-based films: a spectra-microstructure overview. *J. Non-Cryst. Solids* **2003**, 316, 309–319. DOI: 10.1016/S0022-3093(02)01637-X.
35. Pinakov, V.I.; Stoyanovsky, O.I.; Tanashev Yu. Yu.; Pikarevsky, A.A.; Grinberg, B.E.; Dryab, V.N.; Kulik, K.V.; Danilevich, V.V.; Kuznetsov, D.V.; Parmon, V.N. TSEFLAR™ – the centrifugal flash reactor for rapid thermal treatment of powdered materials. *Chem. Eng. J.* **2005**, 107, 157–161. DOI: 10.1016/j.cej.2004.12.026.
36. Kul'ko, E.V.; Ivanova, A.S.; Kruglyakov, V.Yu.; Moroz, E.M.; Shefer, K. I.; Litvak, G. S.; Kryukova, G.N.; Tanashev, Yu. Yu.; Parmon, V. N. Synthesis of aluminum oxides from the products of the rapid thermal decomposition of hydrargillite in a centrifugal flash reactor: II. Structural and textural properties of aluminum hydroxide and oxide obtained from the product of the centrifugal thermal activation of hydrargillite (CTA product). *Kinet. Catal.* **2007**, 48, 316–326. DOI: 10.1134/S0023158407020176.
37. Klinbumrung, A.; Thongtem, T.; Thongtem, S. Characterization of orthorhombic  $\alpha$ - $\text{MoO}_3$  microplates produced by a microwave plasma process. *J. Nanomater* **2012**, 930763. DOI: 10.1155/2012/930763.
38. Dieterle, M.; Weinberg, G.; Mestl, G. Raman spectroscopy of molybdenum oxides - Part I. Structural characterization of oxygen defects in  $\text{MoO}_{3-x}$  by DR UV/VIS, Raman spectroscopy and X-ray diffraction. *Phys. Chem. Chem. Phys.* **2002**, 4, 812–821. DOI: 10.1039/b107012f.
39. Zaitsev, V.B.; Konstantinova, E.A.; Deygen, D.M.; Rummyantseva, M.N.; Podol'ko, E.V.; Pustovalov, M.V.; Kashkarov P.K. Optoelectronic properties of nitrogen and carbon doped nanocrystalline titania. *Moscow University Physics Bulletin* **2013**, 68, 387–396. DOI: 10.3103/S0027134913050160.
40. Abdulkarem, A.M.; Aref, A.A.; Abdulhabeeb, A.; Li, Y.F.; Yu, Y. Synthesis of  $\text{Bi}_2\text{O}_3/\text{Cu}_2\text{O}$  nanoflowers by hydrothermal method and its photocatalytic activity enhancement under simulated sunlight. *J. Alloys Compd.* **2013**, 560, 132–141. DOI: 10.1016/j.jallcom.2013.01.134.
41. Rauf, M.A.; Meetani, M.A.; Khaleel, A.; Ahmed, A. Photocatalytic degradation of Methylene Blue using a mixed catalyst and product analysis by LC/MS. *Chem. Eng. J.* **2010**, 157, 373–378. DOI: 10.1016/j.cej.2009.11.017.
42. Nethercot, A.H. Prediction of fermi energies and photoelectric thresholds based on electronegativity concept. *Phys. Rev. Lett.* **1974**, 33, 1088–1091. DOI: 10.1103/PhysRevLett.33.1088
43. Chandar, N.R.; Agilan, S.; Thangarasu, R.; Muthukumarasamy, N.; Ganesh, R. Influence of the annealing temperature on the formation of  $\text{Mo}_{17}\text{O}_{47}$  and  $\text{MoO}_3$  nanoparticles and their Photocatalytic performances for the degradation of MB dye. *J. Mater. Sci. - Mater. Electron.* **2020**, 31, 7378–7388. DOI: 10.1007/s10854-019-02820-w.

44. Szkoda, M.; Trzcinski, K.; Nowak, A.P.; Gazda, M.; Sawczak, M.; Lisowska-Oleksiak A. The effect of morphology and crystalline structure of Mo/MoO<sub>3</sub> layers on photocatalytic degradation of water organic pollutants. *Mater. Chem. Phys.* **2020**, 248, 122908. DOI: 10.1016/j.matchemphys.2020.122908

## Figures

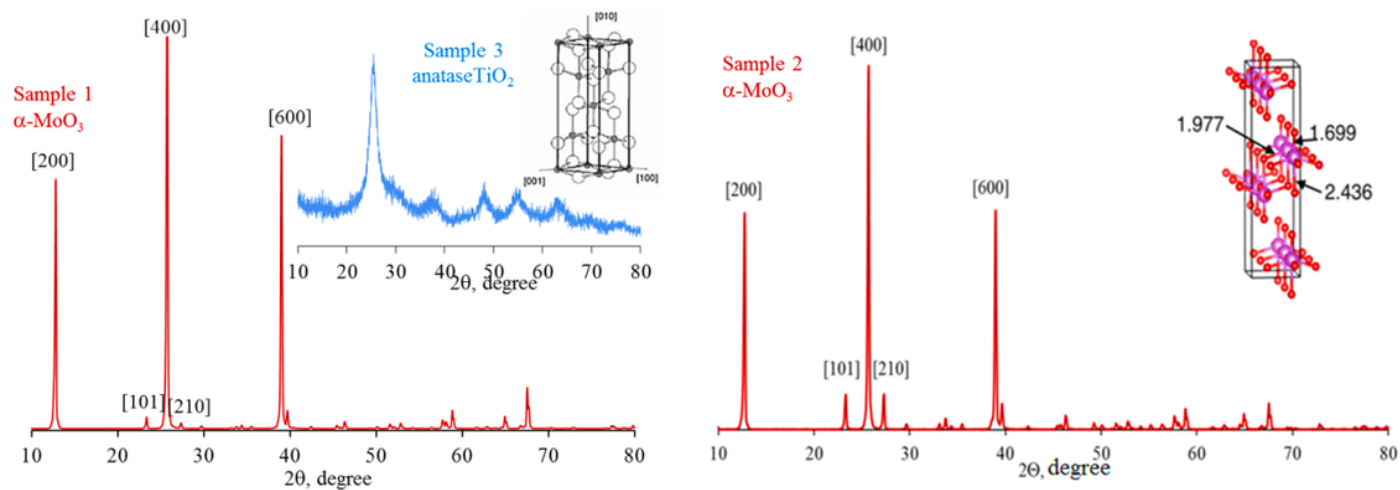


Figure 1

X-ray diffraction patterns of the as-prepared samples:

1: MoO<sub>3</sub>/TiO<sub>2</sub>-SiO<sub>2</sub>; 2: MoO<sub>3</sub>; 3: TiO<sub>2</sub>-SiO<sub>2</sub>

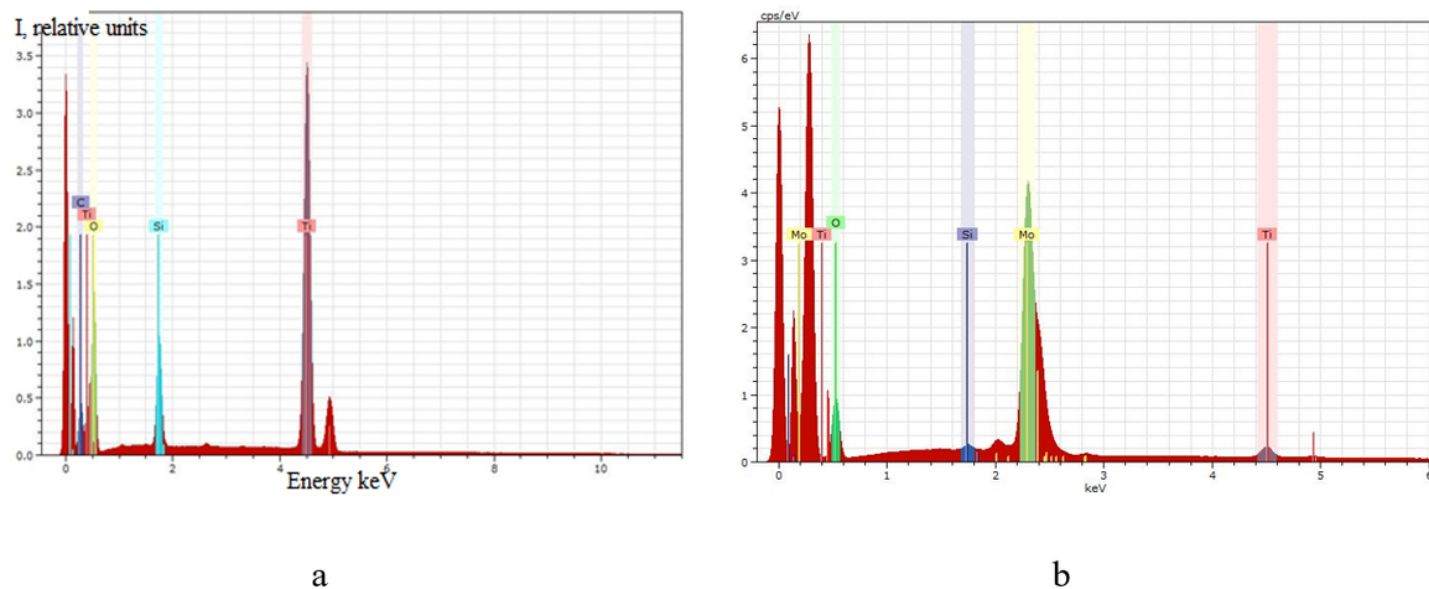
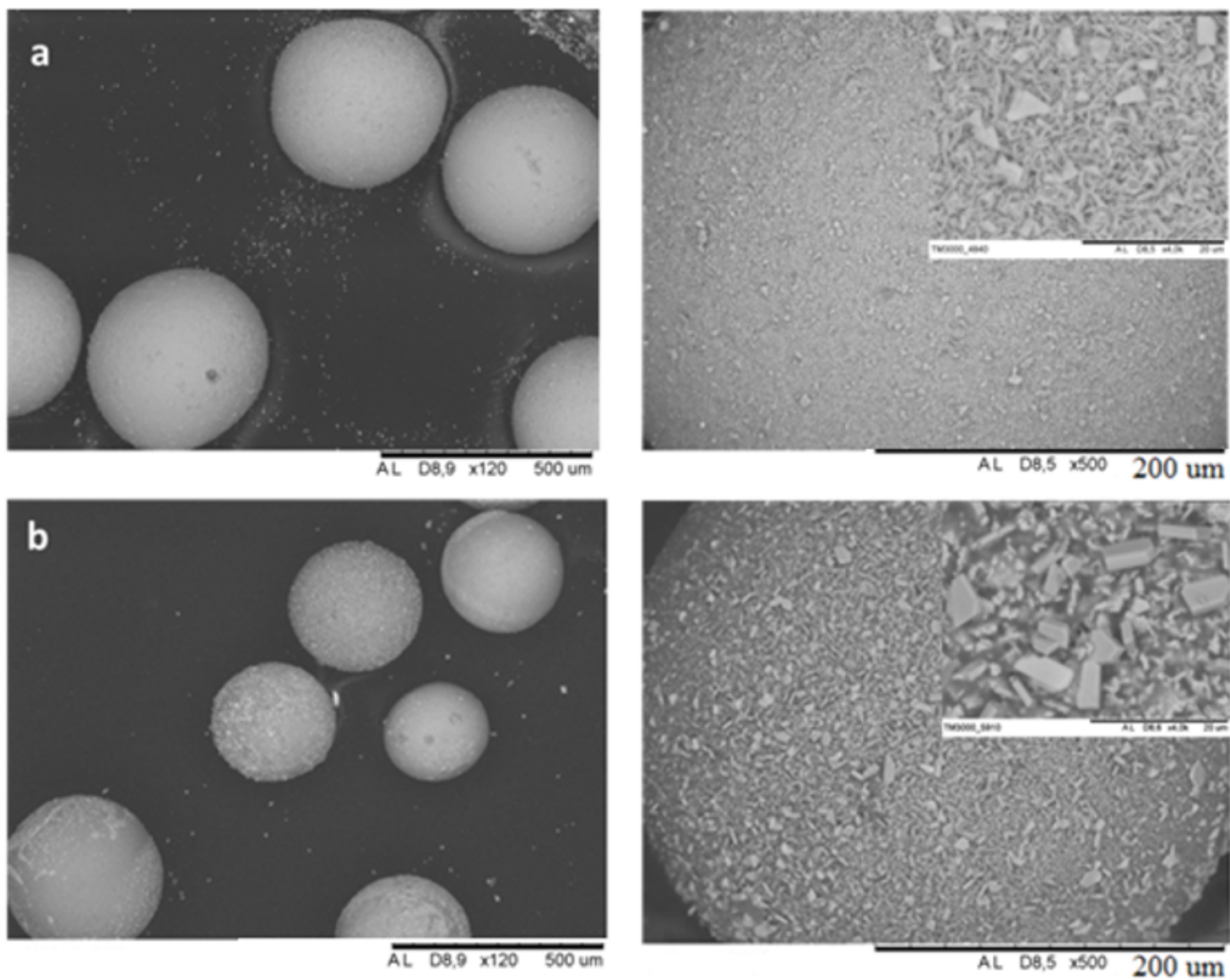


Figure 2

X-ray emission spectra, (a)  $\text{TiO}_2\text{-SiO}_2$  and (b)  $\text{MoO}_3/\text{TiO}_2\text{-SiO}_2$  samples.



**Figure 3**

Scanning electron micrographs of (a)  $\text{MoO}_3$  and (b)  $\text{MoO}_3/\text{TiO}_2\text{-SiO}_2$  samples.

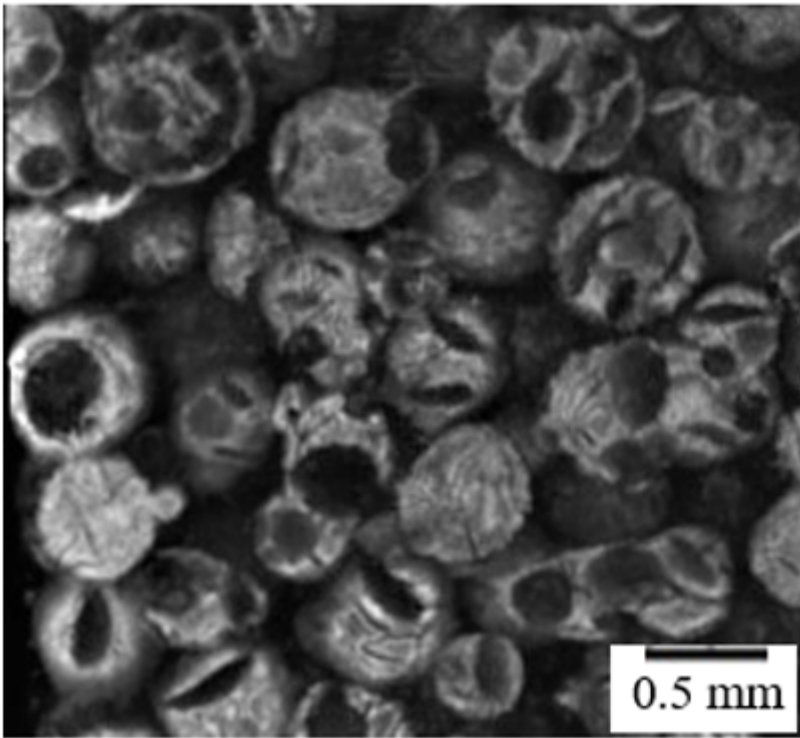


**Figure 4**

Results of 3D microtomography of the  $\text{MoO}_3/\text{TiO}_2\text{-SiO}_2$  composites.

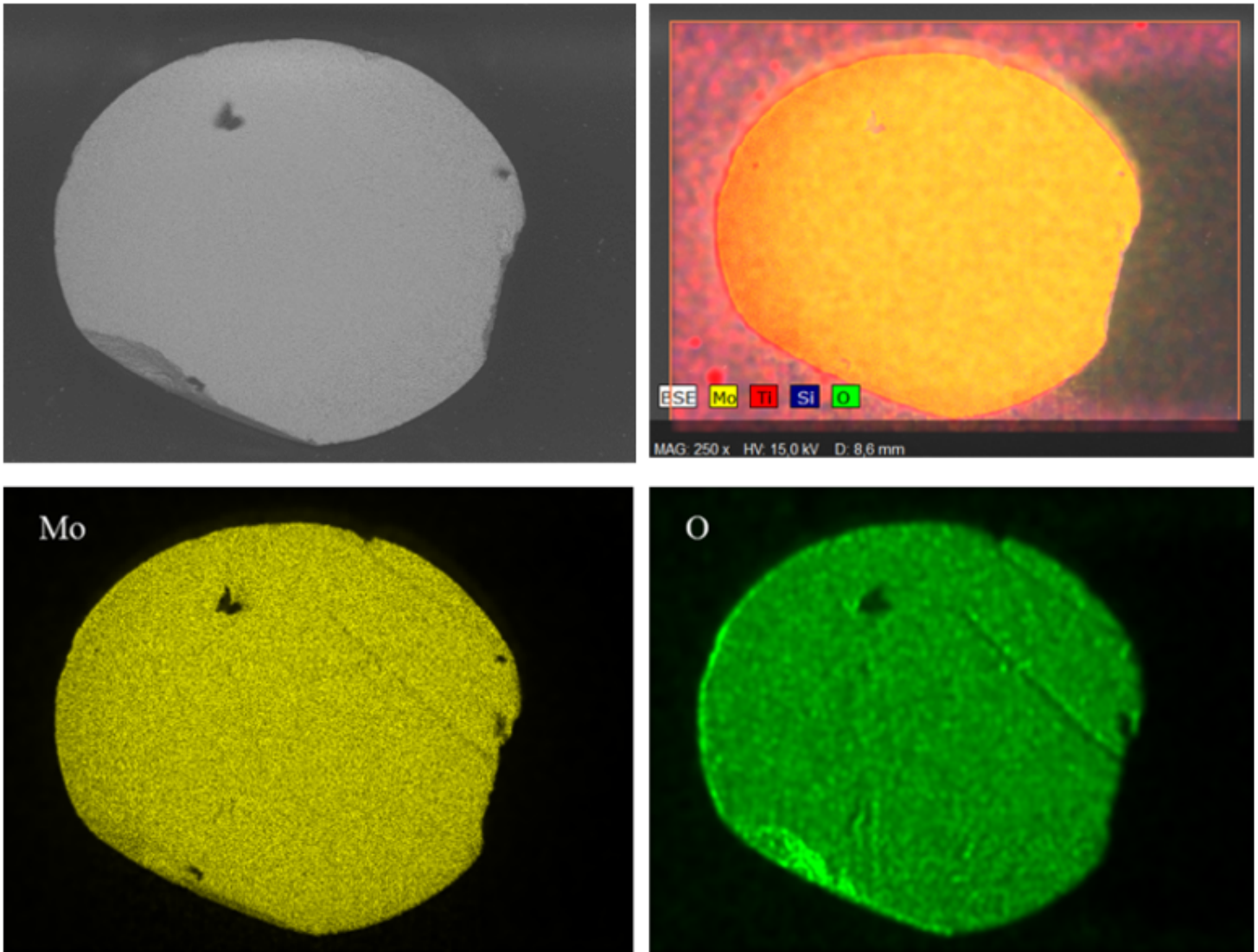


**Figure 5**

Scanning electron micrograph and profile of elements distribution on the surface of  $\text{MoO}_3/\text{TiO}_2\text{-SiO}_2$  composites in section.

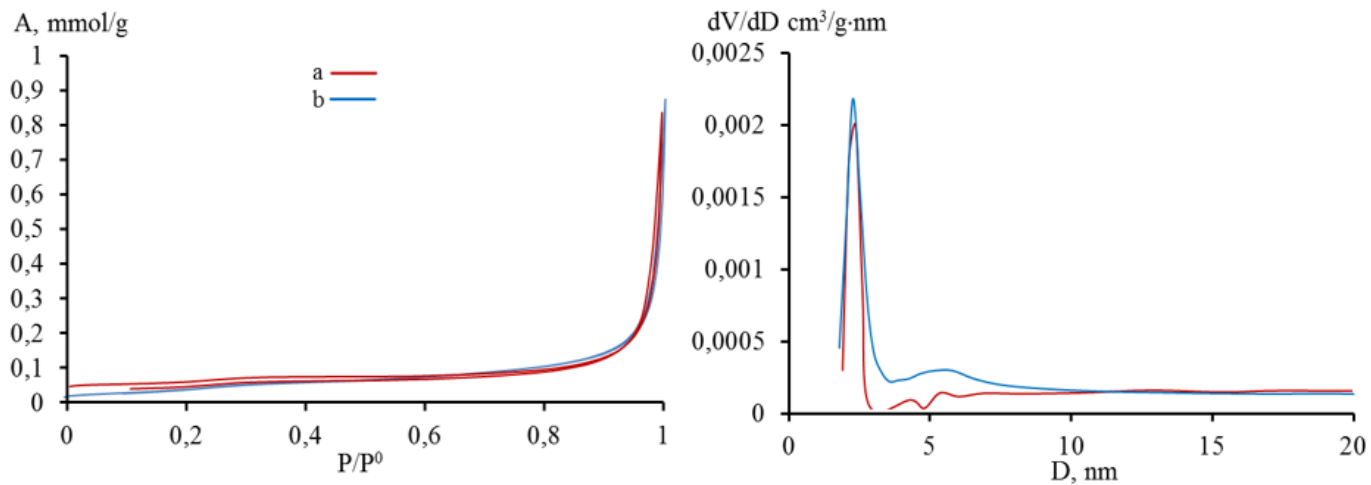


**Figure 6**

The N<sub>2</sub> sorption results of (a) MoO<sub>3</sub> and (b) MoO<sub>3</sub>/TiO<sub>2</sub>-SiO<sub>2</sub> samples.

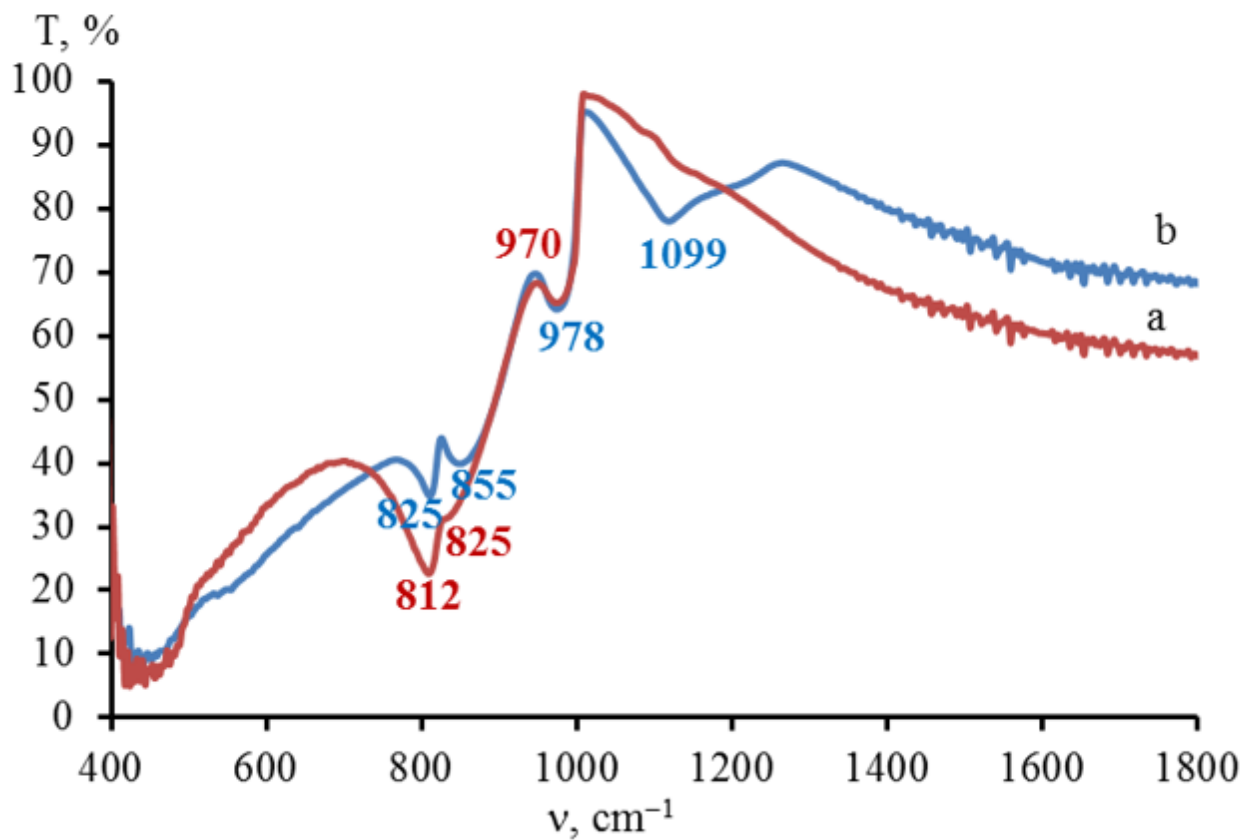


**Figure 7**

IR spectra of (a) MoO<sub>3</sub> and (b) MoO<sub>3</sub>/TiO<sub>2</sub>-SiO<sub>2</sub> samples.

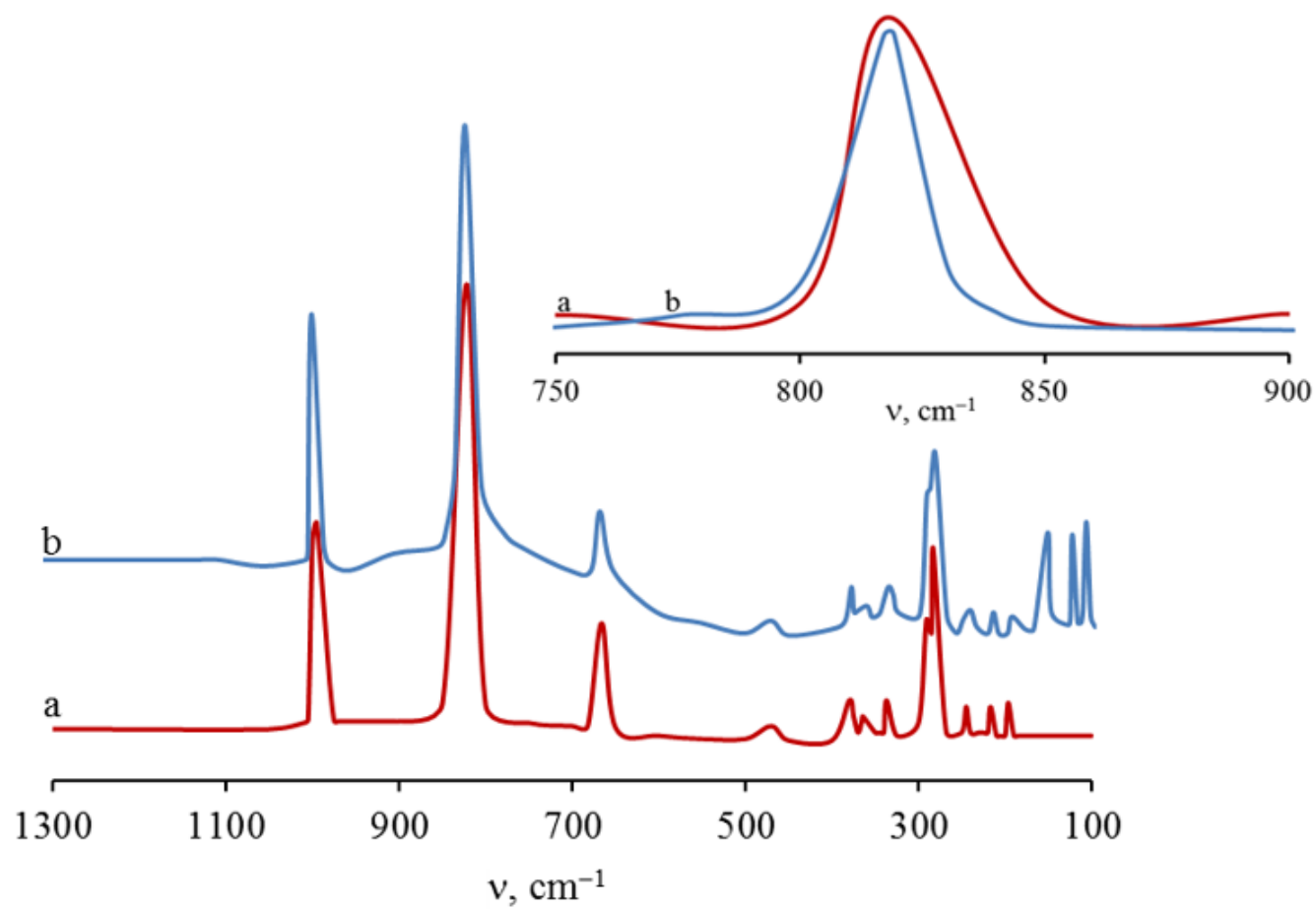


**Figure 8**

Raman spectra of MoO<sub>3</sub> (a) and MoO<sub>3</sub>/TiO<sub>2</sub>-SiO<sub>2</sub> (b) samples

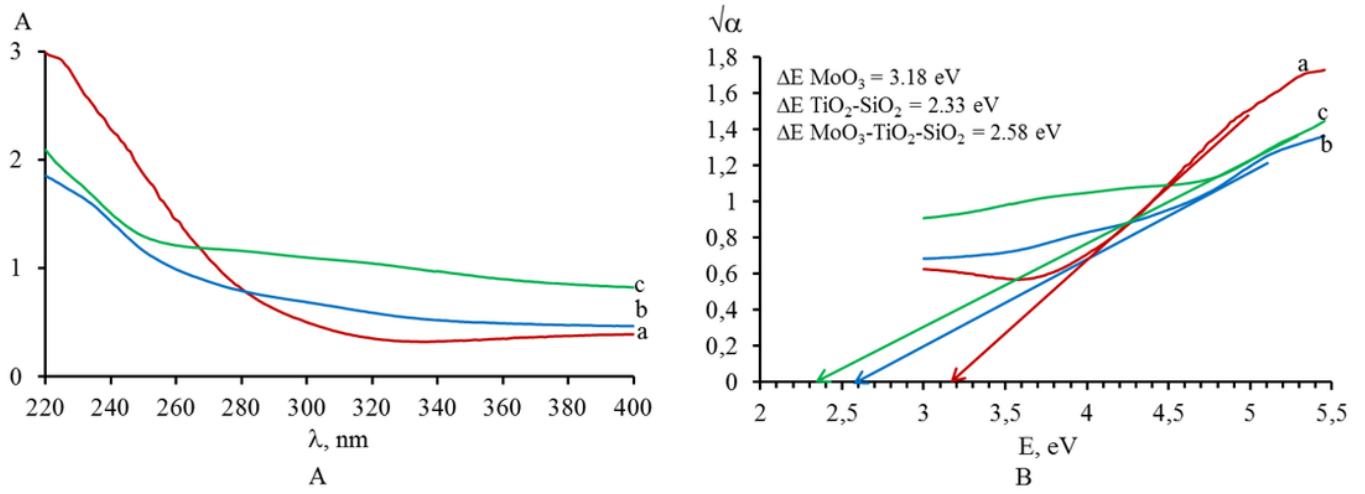


**Figure 9**

(A) absorption spectra, (B) plots of  $(\sqrt{\alpha})$  versus  $(h\nu)$ , (a) MoO<sub>3</sub>, (b) MoO<sub>3</sub>/TiO<sub>2</sub>-SiO<sub>2</sub> and (c) TiO<sub>2</sub>-SiO<sub>2</sub> samples

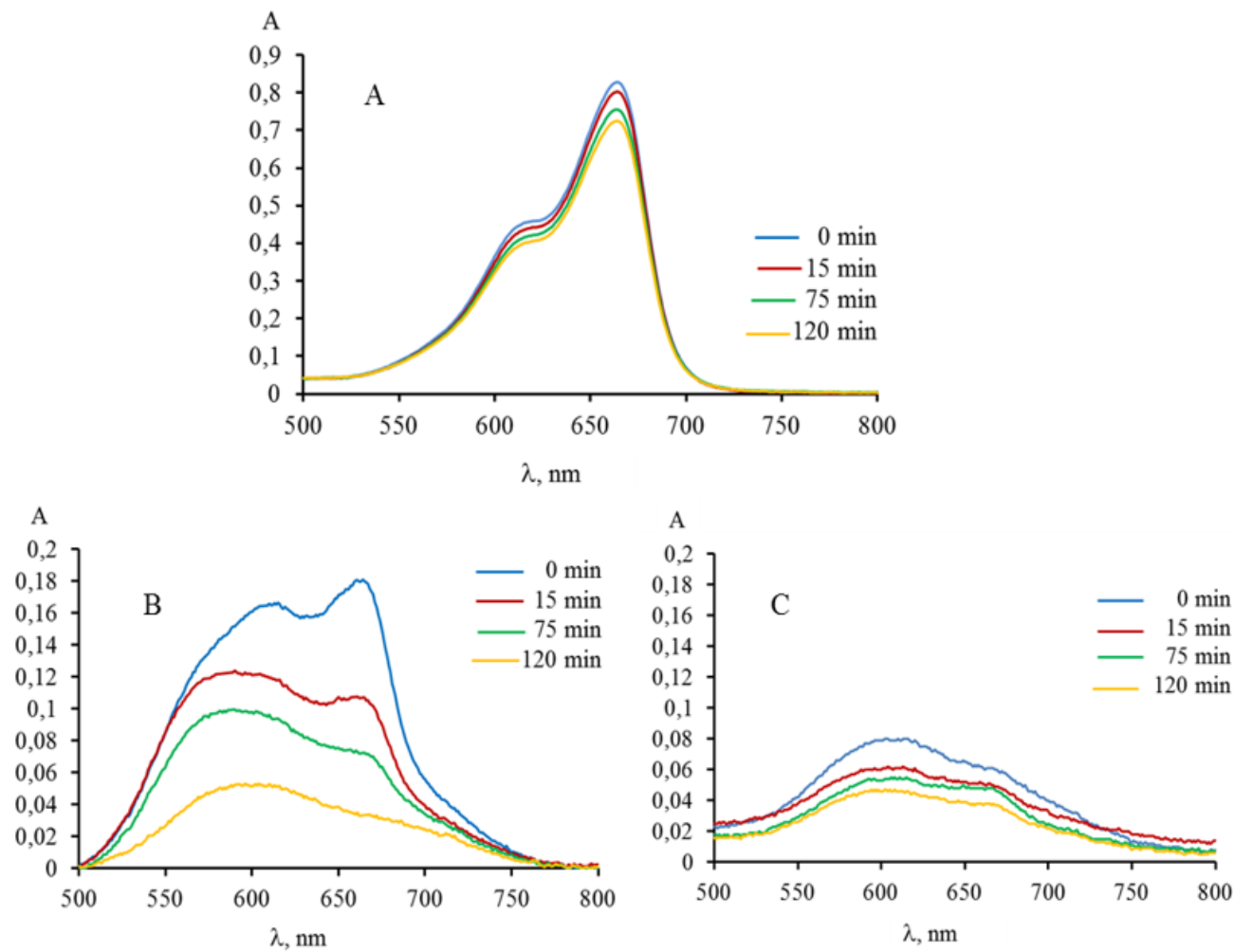


**Figure 10**

Visible absorption spectra of MB solutions after irradiation with UV light lamp ( $\lambda_{\text{max}} = 312 \text{ nm}$ ): pure MB (A), in the presence of  $\text{MoO}_3$  (B) and  $\text{MoO}_3/\text{TiO}_2\text{-SiO}_2$  (C) samples

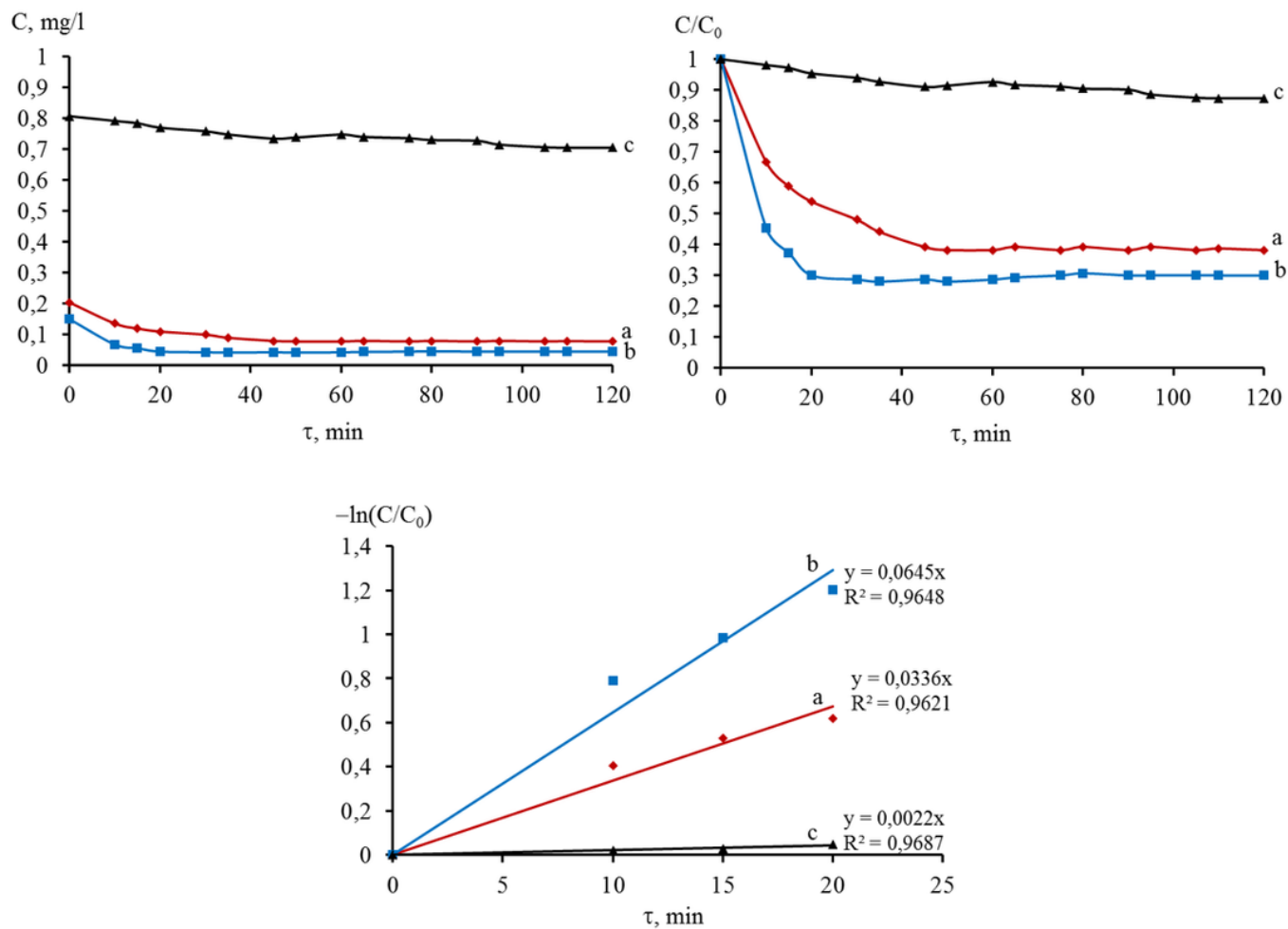


**Figure 11**

The kinetics of the photodegradation of MB solutions ( $[MB] = 5 \text{ mg/l}$ ,  $42 \text{ ml}$ ,  $\lambda = 312 \text{ nm}$ ): MB in the presence of  $\text{MoO}_3$  (a) and  $\text{MoO}_3/\text{TiO}_2\text{-SiO}_2$  (b), pure MB (c)

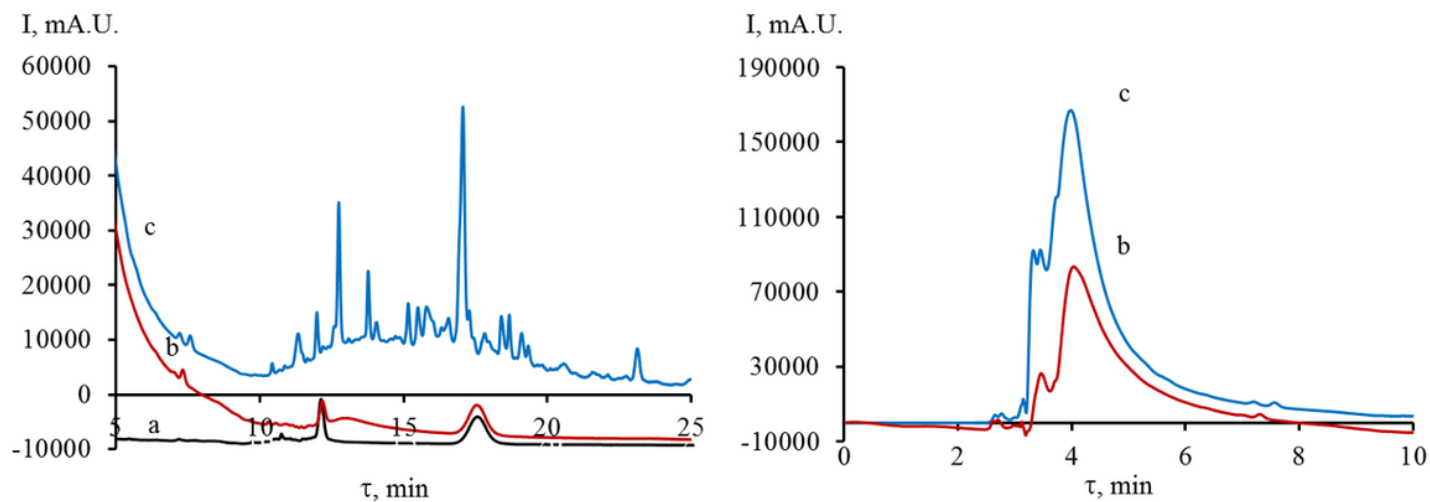


**Figure 12**

HPLC analysis of MB solutions after holding it in the dark in the presence of the catalyst (a)  $\text{MoO}_3$  and after photocatalytic degradation under irradiation at 312 nm in the presence of (b)  $\text{MoO}_3$  and (c)  $\text{MoO}_3/\text{TiO}_2\text{-SiO}_2$ .

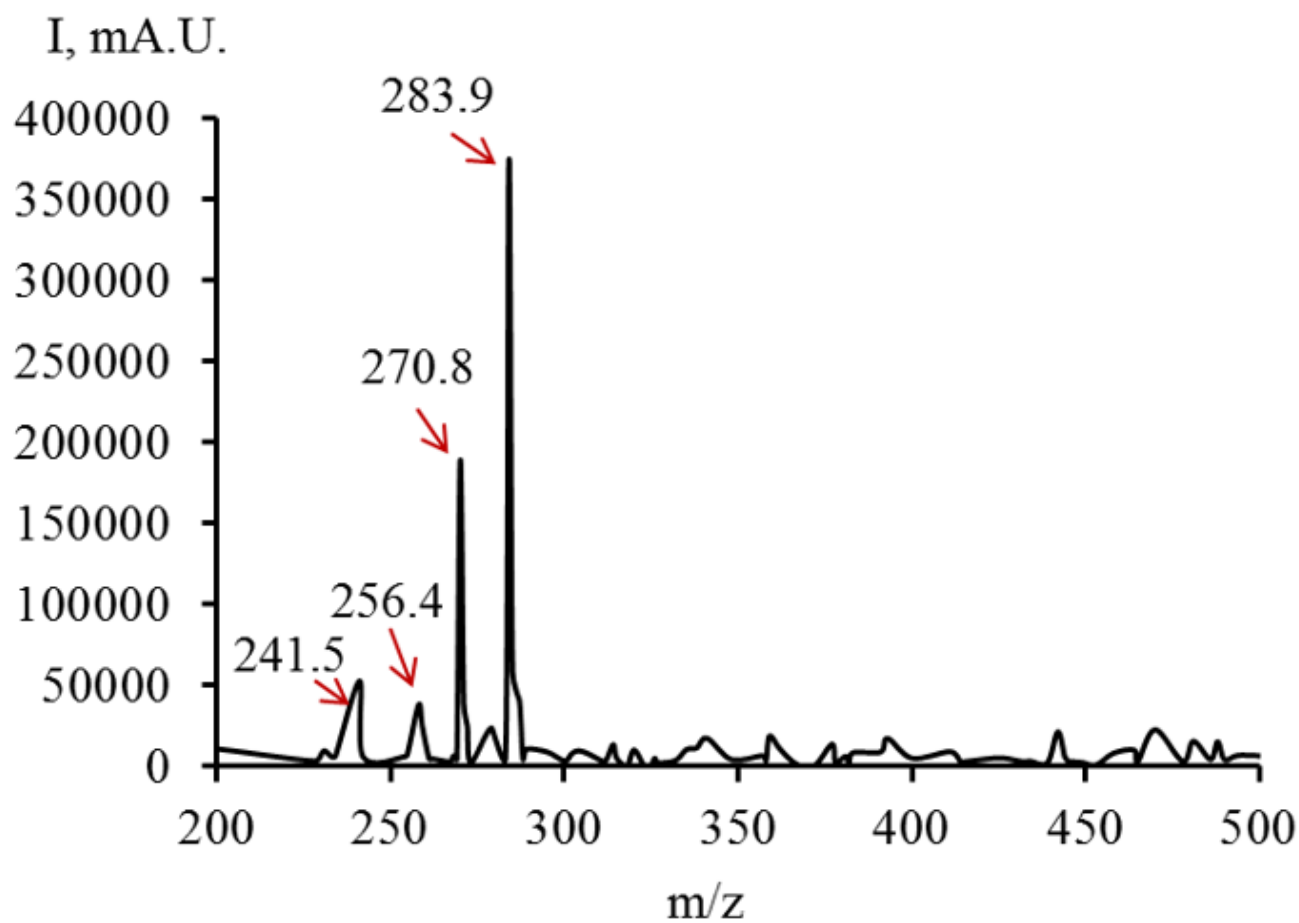


Figure 13

Mass spectrum degradation intermediate products of MB solution after irradiation in the presence of  $\text{MoO}_3/\text{TiO}_2\text{-SiO}_2$  sample

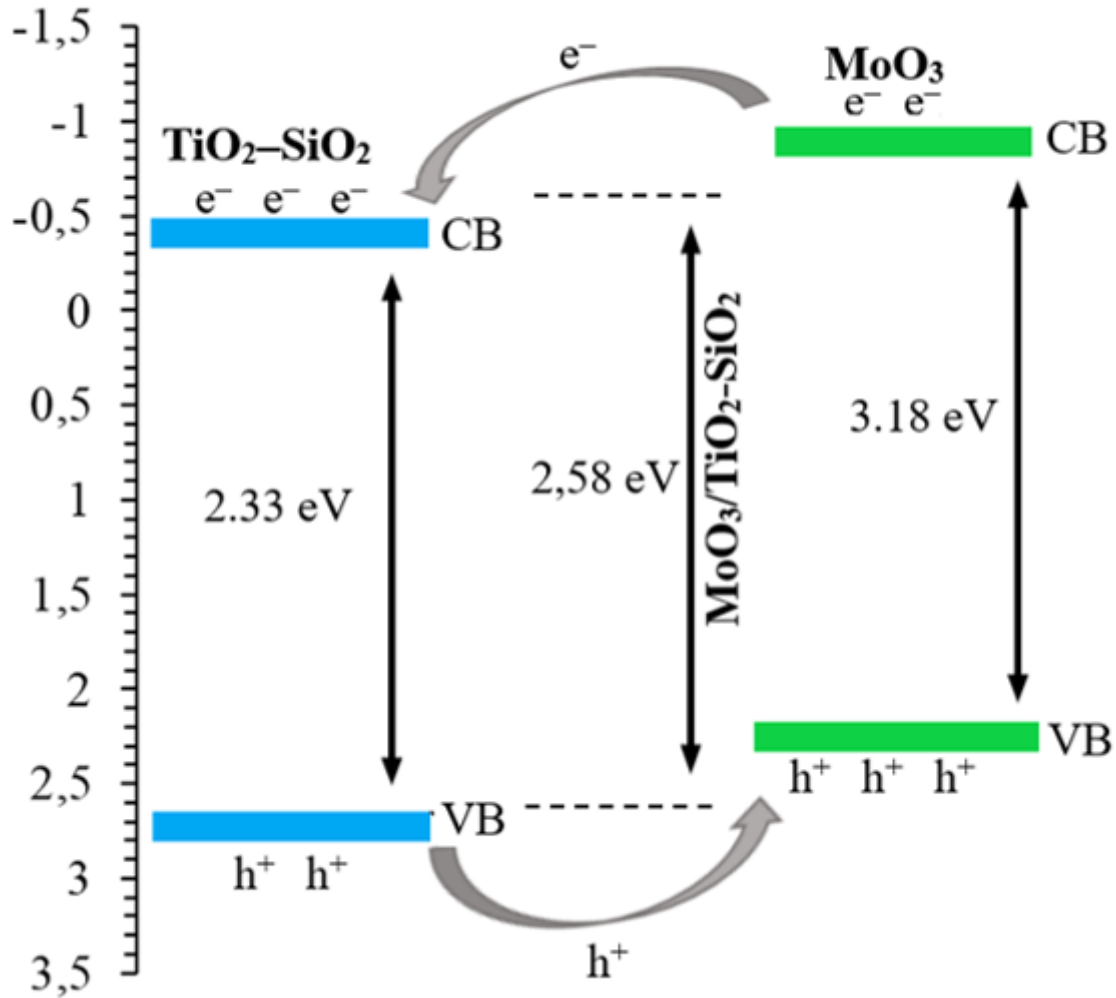


Figure 14

The schematic diagram illustrating the energy band structure and occurrence of vectorial electrons and holes transfer in the  $\text{MoO}_3/\text{TiO}_2\text{-SiO}_2$  composite